



Graphene-wrapped $\text{Ag}_3\text{PO}_4/\text{LaCO}_3\text{OH}$ heterostructures for water purification under visible light

Santosh S. Patil^{a,b}, Mukund G. Mali^c, Animesh Roy^a, Mohaseen S. Tamboli^a, Virendrakumar G. Deonikar^a, Deepak R. Patil^a, Milind V. Kulkarni^a, Salem S. Al-Deyab^d, Sam S. Yoon^{c,*}, Sanjay S. Kolekar^b, Bharat B. Kale^a

^a Centre for Materials for Electronics Technology (C-MET), Department of Electronics and Information Technology (DeitY), Govt. of India, Pune, India

^b Analytical Chemistry and Material Science Laboratory, Department of Chemistry, Shivaji University, Kolhapur, MS India

^c Solar Cell & Aerosol Science Laboratory, School of Mech. Eng., Korea University, Seoul, South Korea and School of Chemical Sciences, Solapur University, Solapur, MS, India

^d Petrochemical Research Chair, Department of Chemistry, King Saud University, Riyadh, Saudi Arabia

ARTICLE INFO

Article history:

Received 8 February 2016

Revised 16 April 2016

Accepted 9 May 2016

Available online 1 June 2016

Keywords:

Ag_3PO_4

LaCO_3OH

Graphene

Heterostructures

Photocatalytic MB degradation

Co-catalyst

ABSTRACT

We demonstrated a unique synthesis approach of graphene (GR)-wrapped $\text{Ag}_3\text{PO}_4/\text{LaCO}_3\text{OH}$ (APO/LCO) heterostructures by an in-situ wet chemical method. FESEM analysis reveals the formation of rhombic dodecahedrons of APO decorated with LCO and later wrapped with GR flakes. Optical studies shows two absorption edges corresponding to the band gap energies of APO (2.41 eV) and LCO (4.1 eV). Considering the absorption edge of the heterostructures in the visible region, the photocatalytic activities of photocatalysts containing different APO/LCO mass ratios were evaluated by the degradation of MB. GR-decorated composite with 20% LCO (APO/LCO20/GR) exhibited the highest photocatalytic activity for MB degradation, with a rate constant, k of 0.541 min^{-1} . The photocatalytic activity of APO/LCO20/GR more greatly enhanced than those of the individual constituents (APO, LCO, APO/LCO20). The enhanced photocatalytic activity of the heterostructure can be attributed to the co-catalytic effect of LCO as well as intriguing physicochemical properties of GR. To understand the enhanced photocatalytic activity of the heterostructures the photocatalytic reaction mechanism is proposed in detail. The recyclability of the APO/LCO/GR composite photocatalyst is further evaluated by reusing the catalyst in replicate photocatalytic experiments which shows consistent photocatalytic activity thereby confirms the stability and reusability of heterostructure photocatalyst.

© 2016 Science Press and Dalian Institute of Chemical Physics, Chinese Academy of Sciences. Published by Elsevier B.V. and Science Press. All rights reserved.

1. Introduction

The recent surge in industrialization has led to a drastic increase in the level of water pollution, which has become a major global concern [1]. Pesticides, dyes, and a variety of chemicals released from the textile, agricultural, and pharmaceutical industries are the main water contaminants [2]. The textile industry uses numerous dyes and is thus the largest source of colored dye effluents. Azo compounds account for 65%–75% of these dye pollutants, and it is estimated that about 12% of the dye utilized in these industries is lost annually during the textile manufacturing and processing operations [3]. The direct discharge of these colored dyes into the environment without treatment creates severe

environmental pollution problems as toxic and potentially carcinogenic substances are released into the aquatic media [1–3]. Hence, the disposal of wastewater is a worldwide environmental concern and its treatment is of the utmost importance. The conventional methods such as precipitation, adsorption by activated carbon, air stripping, coagulation are mostly ineffective for destroying dyes. In comparison the low-cost and environmentally friendly process of semiconductor photocatalysis appears to be a viable method for destroying dyes [3,4]. One of the key objectives in this field is to develop high efficiency photocatalyst materials that can efficiently utilize sunlight as the energy source [5]. Thus far, various visible light active photocatalysts have been developed, such as NiS/CdS [6], ZnInS₄ [7], AgO/Ag₂Mo₂O₇ [8], CdInS₄ [9], and TiO_{2-x}N_x [10]. However, the efficiency of these photocatalysts is still too low for industrial application, and therefore materials with high efficiency and long-term stability are still being actively sought [11].

* Corresponding author.

E-mail addresses: skyoons@korea.ac.kr (S.S. Yoon), sskolekar@gmail.com (S.S. Kolekar), bbkale@cmet.gov.in (B.B. Kale).

Recently, Yi and co-workers reported silver orthophosphate (Ag_3PO_4), a visible light responsive photocatalyst that can achieve a quantum efficiency of up to 90% for water oxidation as well as for decomposition of organic dyes [12]. The photocatalytic response of this novel Ag_3PO_4 photocatalyst is dozens of times faster than that of commercial TiO_2-xN_x [13]. Unfortunately, the low structural stability and large crystallite size of Ag_3PO_4 (0.5–2 μm) have remained major hindrances, limiting its photocatalytic performance and large scale practical applications [14]. To enhance the properties of Ag_3PO_4 , structural modification has been pursued with the development of various morphologies such as spheres [15], rhombic dodecahedrons [16], concave microcrystals [17] and tetrahedrons, cubes, 2D dendritic morphologies, nanorods, tetrapods [18], and flower-like nanospheres. These studies conclude that the surface-active facets with different energies strongly influence the photocatalytic activity. For example, Bi et al. reported that Ag_3PO_4 with a rhombic dodecahedron morphology and exposed active (110) facets exhibits higher activity than its cubic congeners with exposed (100) facets in the degradation of rhodamine B (RhB) [12]. Similarly, Ag_3PO_4 composite photocatalyst systems, such as $\text{TiO}_2/\text{Ag}_3\text{PO}_4$ [19], $\text{Ag}_3\text{PO}_4/\text{NiFe}_2\text{O}_4$ [20], $\text{Ag}_3\text{PO}_4/\text{BiOI}$ [21], $\text{ZnFe}_2\text{O}_4\text{-ZnO-Ag}_3\text{PO}_4$ [22], Ag_3PO_4 glass nanocomposites [23], $\text{Ag}_3\text{PO}_4/\text{TiO}_2/\text{graphene}$ [24], $\text{Ag}_3\text{PO}_4/\text{AgI}$ [25], and $\text{Ag}_3\text{PO}_4/\text{Cr-SrTiO}_3$ [26] have been adopted to exhibit improved charge separation, structural stability, and photocatalytic activity relative to bare Ag_3PO_4 . In light of these accomplishments, herein, we couple Ag_3PO_4 with LaCO_3OH to generate a $\text{Ag}_3\text{PO}_4/\text{LaCO}_3\text{OH}$ (APO/LCO) heterostructure photocatalyst. This approach exploits the combination of a wide band gap semiconductor with a narrow band gap semiconductor and seeks to identify the parameters that affect the physicochemical properties as well as the photocatalytic activity. Since, both the conduction band minimum (CBM) and valence band maximum (VBM) of LaCO_3OH are negative compared to those of Ag_3PO_4 , various oxidation reactions can be initiated in the APO/LCO composite [27,28]. In addition, carbon based materials such as $g\text{-C}_3\text{N}_4$, graphene (GR) are also recognized as a large surface area materials with high electronic conductivity and with scope for tailored morphologies. Therefore, constructing a composite with these materials should facilitate the resolution of several issues during the photocatalytic process [5]. Recently, significant work has been carried out on $\text{Ag}_3\text{PO}_4/\text{GR}$ [29–31] and $\text{Ag}_3\text{PO}_4/g\text{-C}_3\text{N}_4$ [32–35] composites for water splitting and organic pollutant remediation applications.

Herein, we demonstrate the synthesis of the APO/LCO/GR composite photocatalysts via the in situ wet chemical method. With varying the mass ratio of LCO and graphene in the APO/LCO/GR composite photocatalyst, the photocatalytic activity of the composites is evaluated for degradation of methylene blue (MB). From pre-screening evaluations, APO/20% LCO was found to be an optimal composition for MB degradation, and this composition was further selected for graphene incorporation. The experimental results confirm that compared to the bare Ag_3PO_4 and LaCO_3OH photocatalysts, the APO/LCO/GR composite exhibits superior photocatalytic activity and enhanced stability.

2. Experimental

The commercial chemicals lanthanum (III) nitrate hexahydrate ($\text{La}(\text{NO}_3)_3 \cdot 6\text{H}_2\text{O}$; Qualigen Chemicals Ltd.), urea (NH_2CONH_2 ; Qualigen Chemicals Ltd.), silver nitrate (AgNO_3 ; SDFCL), ammonium dihydrogen phosphate ($\text{NH}_4\text{H}_2\text{PO}_4$; Qualigen Chemicals Ltd.), natural graphite (Loba Chemicals), sodium nitrate (NaNO_3 , 99%; Fisher Scientific), potassium permanganate (KMnO_4 , 99%; SDFCL), and hydrogen peroxide (H_2O_2 , 30%; Fisher Scientific) were all of

analytical reagent (AR) grade and were used without further purification.

2.1. LaCO_3OH synthesis

LaCO_3OH powder was synthesized via a one-step hydrothermal method using $\text{La}(\text{NO}_3)_3 \cdot 6\text{H}_2\text{O}$ and urea (NH_2CONH_2) in a 1:6 molar ratio. $\text{La}(\text{NO}_3)_3 \cdot 6\text{H}_2\text{O}$ (0.866 g) and NH_2CONH_2 (0.720 g) were separately dissolved in 80 mL of distilled water and mixed together. The solution (pH of 6) was stirred for 10 min at room temperature and transferred into a Teflon lined stainless steel autoclave. The autoclave was kept in an oven at 180 °C for 24 h. The as-obtained precipitates were then washed thoroughly with deionized distilled water and ethanol and allowed to dry overnight at 50 °C.

2.2. $\text{Ag}_3\text{PO}_4/\text{LaCO}_3\text{OH}/\text{graphene}$ synthesis

Synthesis of the APO/LCO heterojunction photocatalyst was carried out by an in situ wet chemical method. The requisite amount of LCO powder was dispersed in 20 mL of distilled water and ultrasonicated for 10 min. Subsequently, $\text{NH}_4\text{H}_2\text{PO}_4$ solution (4.8 mmol) was added and ultrasonicated for 5 min. An aqueous solution of AgNO_3 (8.9 mmol) was then added dropwise under vigorous magnetic stirring (having pH of 3) and kept under the same conditions for 4 h. The as-obtained composite powder was meticulously washed with distilled water, dried, and used for further characterization. The APO/(x% LCO) composites (where x% is the nominal mass ratio of LCO to APO) with mass ratios of $x = 5\%$, 10%, and 15% were synthesized using the same process. The prepared samples are hereafter denoted as: APO, LCO, APO/LCO5 (APO/5% LCO), APO/LCO10 (APO/10% LCO), APO/LCO15 (APO/15% LCO), APO/LCO20 (APO/20% LCO), and APO/LCO25 (APO/25% LCO). For preparation of the $\text{Ag}_3\text{PO}_4/\text{LaCO}_3\text{OH}/\text{GR}$ composite, a reaction similar to that used for $\text{Ag}_3\text{PO}_4/\text{LaCO}_3\text{OH}$ (APO/LCO20%) was performed, but with the addition of graphene oxide (GO) and hydrothermal treatment. Graphene oxide (GO) was prepared from natural graphite using a modified Hummer's method [36]. First, GO (1 mg/mL) was dispersed in distilled water and ultrasonicated for 2 h to exfoliate the GO sheets. The reaction precursor (similar to APO/LCO20) was directly added to the GO suspension, mixed well under magnetic stirring, and the entire reaction mixture was transferred into a Teflon autoclave and kept in an oven at 180 °C for 12 h. The APO/LCO/GR composite product was washed thoroughly with water and further used for characterization.

2.3. Photocatalytic degradation of dye

Methylene blue (MB), with a major absorption band at 663.89 nm, was chosen as a model pollutant for testing the photocatalytic activities of LCO, APO, APO/LCO and APO/LCO/GR composites. The photocatalytic degradation of MB dye with a concentration of 10 ppm was performed in an aqueous solution using a 300 W Xe lamp ($\lambda \geq 420$ nm) as the light source. The photocatalytic reaction was performed in a custom water-cooled borosilicate glass reactor capable of maintaining the solution at 25 °C. A photocatalyst sample of ~ 10 mg was dispersed in an aqueous solution of MB (50 mL) for every irradiation test. Prior to irradiation, the suspension was magnetically stirred under dark conditions for 90 min to establish an adsorption-desorption equilibrium between the photocatalyst and MB. The solution was then irradiated under magnetic stirring. Aliquots of 3 mL were drawn and filtered at regular intervals of 10 min. The MB concentration in the filtrate was measured using UV-vis spectroscopy. The initial absorbance peak in-

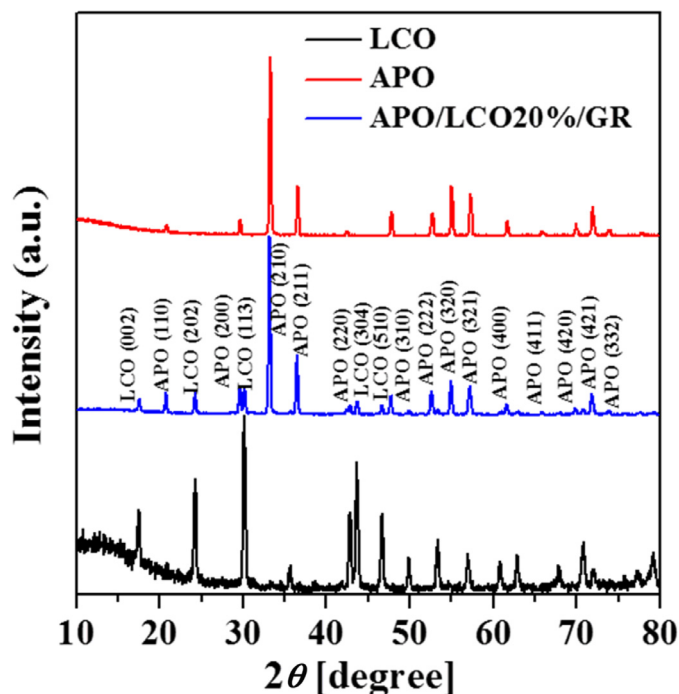


Fig. 1. XRD patterns of LCO, APO, and APO/LCO/GR composite.

tensity of the solution at 663.89 was monitored to evaluate the MB degradation.

2.4. Structural characterization

The phase formation in the composites was investigated via powder X-ray diffraction (XRD) using a Bruker-AXS XRD-D8 Advance. The morphological features of the composites were investigated by field emission scanning electron microscopy (FE-SEM; Hitachi, S-4800 II, Japan). The absorbance spectra of the samples were recorded by a UV–vis spectrometer (Lambda 950 spectrometer, Perkin-Elmer) in the range of 300–900 nm. A photoluminescence study was performed using a Fluorolog-3 Spectrofluorometer (Horiba Scientific) with excitation wavelength 330 nm. Microstructure analysis was conducted using field emission transmission electron microscopy with a JEOL JSM 2200 FS

microscope operating at 200 kV. The Raman spectrum of the samples was obtained using an HR 800-Raman Spectroscopy (Horiba JobinYvon, France). The surface chemical composition was studied by X-ray photoelectron spectroscopy (XPS, Theta Probe, Thermo Fisher Scientific Inc.).

3. Results and discussion

3.1. Structural, morphological and optical properties

Fig. 1 shows the X-ray diffraction patterns (XRD) of APO, LCO, and APO/LCO/GR composite. The XRD pattern of APO/LCO/GR confirms the presence of LCO by observing the relevant peaks that readily indexed as the planes of hexagonal LCO (JCPDS-12,601,615). The other diffraction peaks correspond to the body centered cubic phase of APO (JCPDS file No. 06-0505). No characteristic diffraction peak of GR was observed in the XRD pattern of the APO/LCO/GR composite. This might be due to the weak diffraction intensities of GR compared to those of Ag_3PO_4 and LCO or due to the low amount of graphene oxide employed in the reaction.

Raman spectroscopy is an important tool for investigating the detailed structure of carbon-based composite materials. Fig. 2(a) shows the Raman spectrum of pure APO, pure LCO, APO/LCO20 and APO/LCO20/GR composites whereas Fig. 2(b) depicts the Raman spectra of GO and APO/LCO20/GR photocatalyst samples. The peak observed at around 908 cm^{-1} is characteristic peak of Ag_3PO_4 . In the spectrum of APO/LCO20/GR, some weak peaks were detected in the $200\text{--}1200\text{ cm}^{-1}$ spectral range, and are attributed to Ag_3PO_4 . Based on group theory analysis conducted in previous studies, the weak peak at 345 cm^{-1} is ascribed to the bending vibration of the tetrahedral PO_4 ionic group; the two broad Raman shifts centered at 548 cm^{-1} and 694 cm^{-1} are due to the symmetric stretch of the P–O–P bonds; the higher wavenumber band located at 995 cm^{-1} corresponds to the motion of terminal oxygen bond vibrations in the phosphate chains. Moreover, two distinct bands appear at 1351 cm^{-1} and 1600 cm^{-1} are indexed to be the D and G bands of graphene, respectively [24]. The D band at 1355 cm^{-1} is ascribed to the breathing modes of rings or the k-point phonon of A1g symmetry, while the G band at 1593 cm^{-1} is ascribed to the in-plane bond-stretching vibration of the sp^2 -bonded carbon atoms in a two dimensional hexagonal lattice [36]. Although the pure LCO shows the peak around 1100 cm^{-1} in the Raman spectrum, this peak is not observed in both the APO/LCO20 and APO/LCO/GR heterostructures.

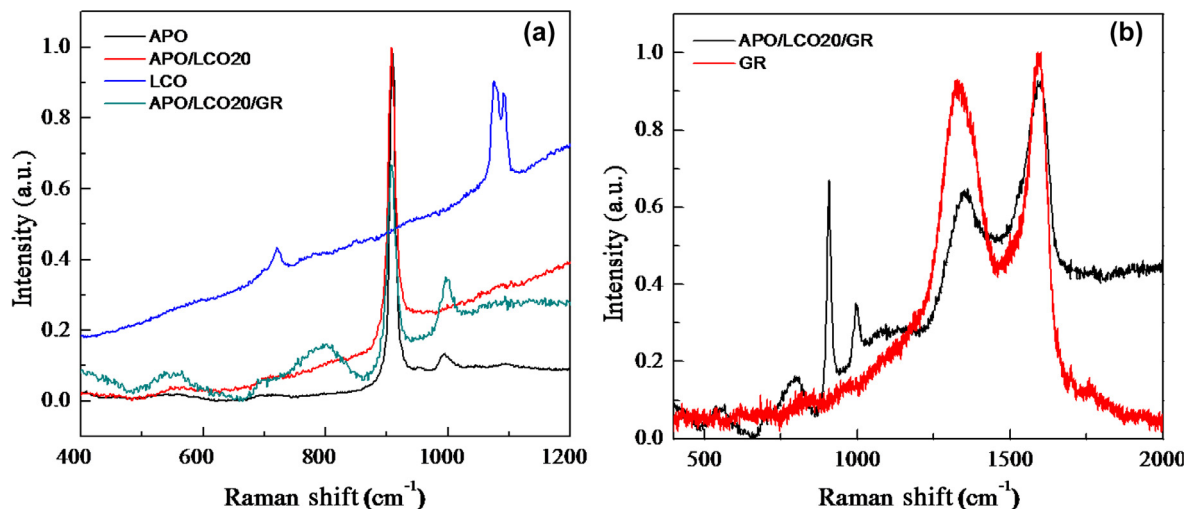


Fig. 2. (a) Raman spectra of APO, LCO and APO/LCO/GR composite, (b) Raman spectra of GR and APO/LCO/GR composite.

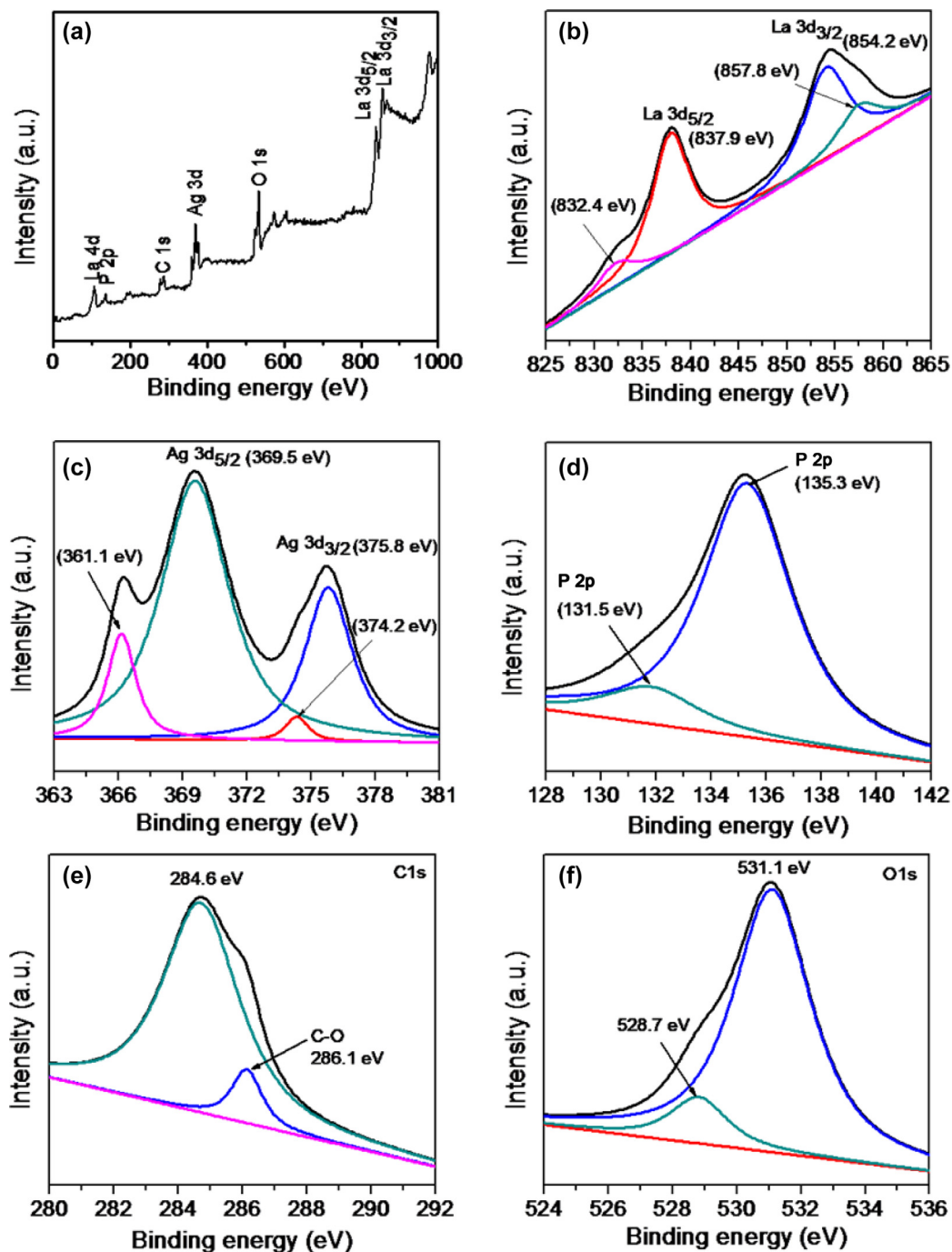


Fig. 3. XPS spectra of APO/LCO/GR composite. (a) Survey spectrum, (b) La 3d, (c) Ag 3d, (d) P 2p, (e) C 1s, (f) O 1s.

The surface components of the APO/LCO20/GR heterojunction were determined by XPS, and the results are displayed in Fig. 3. The survey spectrum (Fig. 3a) shows all the relevant peaks of Ag, P, La, O, and C, confirming the presence of all elements in the composite. The XPS spectrum of La 3d is shown in Fig. 3(b). The binding energy values at 837.9 eV and 854.2 eV correspond to the main peaks of La 3d_{5/2} and La 3d_{3/2}. Two shake-up peaks are also observed at 832.4 eV and 857.8 eV which correspond to the La (III) oxidation state. The binding energy peaks related to Ag 3d_{5/2} and Ag 3d_{3/2} states appeared at 369.5 eV and 375.8 eV, respectively (Fig. 3c). Energy bands located at 369.5 eV and 375.8 eV were attributed to Ag⁺ [37], and those at 361.1 eV and 374.2 eV were attributed to Ag⁰ species [38]. The P 2p spectrum exhibits

the peaks at 131.5 eV and 135.3 eV corresponding to the states of phosphorus (Fig. 3d). The C 1s spectrum (Fig. 3e) exhibits the peaks at 286.1 eV and 284.6 eV, corresponding to the carbonate and carbon [27]. The peaks observed at 531.1 eV and 528.7 eV are ascribed to the 1s orbital of oxygen (Fig. 3f).

The morphological features of APO, LCO, APO/LCO, and APO/LCO/GR composites were examined using FESEM. Fig. 4(a) depicts the FESEM micrographs of pure Ag₃PO₄, illustrating the formation of submicron-sized rhombic dodecahedrons (1.5–3.0 μm). During the synthesis reaction, Ag⁺ slowly reacts with PO₄²⁻ to form APO. The different surface energies of crystalline facets strongly influence the shape, structure, and photocatalytic performance of the material. In particular, the crystallographic study con-

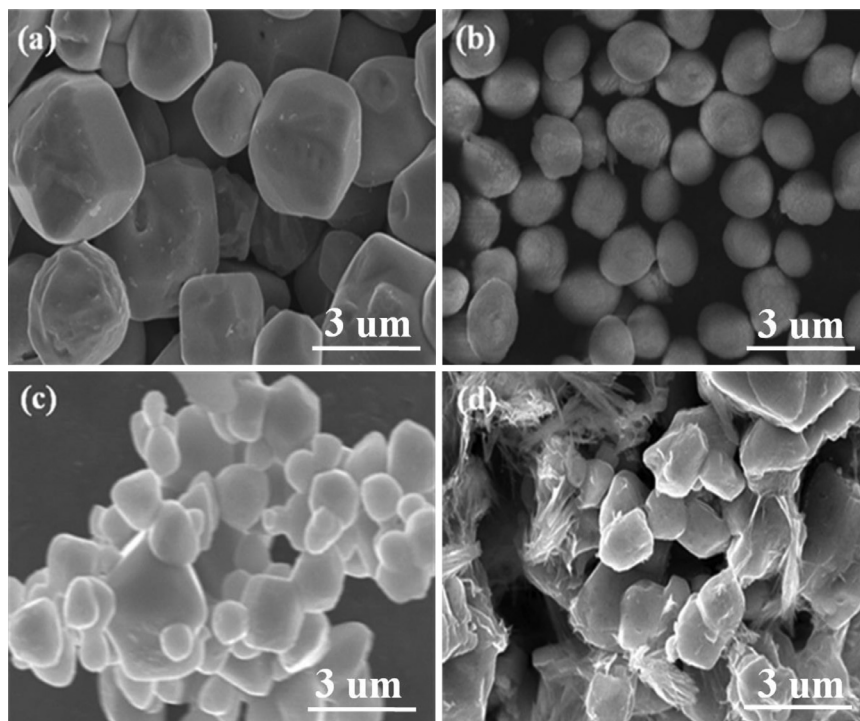


Fig. 4. FESEM images of (a) APO, (b) LCO, (c) APO/LCO, and (d) APO/LCO/GR composite.

ducted by Bi *et al.* suggested that the sequence of facets of APO can be listed in order of increasing surface energy as $g(111) < g(100) < g(110)$ [39].

Among the crystallographic facets of APO, the (110) facet exhibits lower atomic density and higher surface energy promoting the formation of more open sites for attachment to foreign molecule than those offered by the more thermodynamically stable (111) facet. Therefore, during the course of the chemical reaction, irregularly shaped APO structures become aggregated along the (110) crystallographic direction, which results in the formation of rhombic dodecahedrons of APO [20]. Furthermore, pure LCO shows uniform, spherical grape-like microspheres of 1–1.5 μm in diameter (Fig. 4b). Under hydrothermal conditions, La ions react with the carbonyl groups of urea, forming LCO nuclei. These nuclei further grow via Ostwald ripening mechanism. Fig. 4(c) shows the structures of both APO and LCO, indicating the formation of APO/LCO composite structures. More FESEM images are provided in the supporting information (please see Figure S1). The APO dodecahedrons are formed simultaneously with LCO microspheres. Notably, the LCO microspheres are located on the APO dodecahedral facets. LCO is in intimate contact with the surface of APO by weak Vander Waals forces. More significantly, in the APO/LCO/GR sample (Fig. 4d), well-dispersed APO/LCO microcrystals wrapped in graphene sheets are observed.

Further, to confirm the crystallographic structure and particle size of the APO/LCO/GR composite, transmission electron microscope (TEM) images were acquired (Fig. 5). The low resolution TEM images are shown in Fig. 5(a–c) whereas a high resolution TEM image is shown in Fig. 5(d). The TEM analysis reveals that LCO particles are in intimate contact with APO and further graphene sheets are wrapped to the APO/LCO structures. The high resolution TEM (HRTEM) image of the APO/LCO sample (Fig. 5d) clearly showed two distinct sets of lattice fringes. The uniform lattice fringes with interplanar spacing of 0.305 nm and 0.297 nm correspond to the (200) and (113) crystallographic planes of APO and LCO, respectively, indicating the formation of the APO/LCO/GR heterojunction photocatalyst. The interface of APO/LCO heterojunction is shown

by curve dashed line in Fig. 5(d). The corresponding fast-Fourier-transform (FFT) images (Fig. 5f and g) show periodic bright spots, in agreement with the data for APO and LCO, respectively. The chemical composition of APO/LCO20/GR composite was studied using energy dispersive X-ray spectroscopic analysis (EDS, Fig. 5e). The inset table summarizes the observed wt% of C, O, P, Ag, and La, confirming the presence of these elements in the composite structures.

The optical properties of APO, LCO, and the APO/LCO/GR composite materials were studied by UV–vis absorption spectroscopy (Fig. 6). The UV–vis spectra exhibit two absorption edges, indicating the formation of the composite structures. The profile of pure APO showed an absorption edge around ~ 520 nm that corresponds to the band gap energy of 2.46 eV, whereas an absorption edge around 310 nm was observed for LCO with a band gap energy of 4.1 eV. The spectrum of APO indicates that APO can absorb the components of sunlight in the wavelength range below 530 nm; this factor plays a crucial role in determining the photocatalytic performance of the catalyst, especially for degradation of organic pollutants. As the LCO was introduced, the absorption of light with a wavelength of less than 500 nm was slightly depressed, as evidenced from the UV–vis spectra. This is due to the decrease in the relative content of APO in the composite. However, the slight decrease in the absorption of APO/LCO20 compared to pure APO could be attributed to the smaller absorption of LCO and complementary effect of composite. Moreover, on introduction of graphene (APO/LCO20) have not a significant change in absorption as evidenced from spectrum.

To investigate the radiative recombination and separation efficiency of the photogenerated e^-/h^+ pairs in the as-prepared photocatalysts, the photoluminescence (PL) spectra were acquired. It is widely accepted that lower the PL intensity of photocatalyst, lower is the recombination rate of e^-/h^+ . Fig. 7 displays the PL spectra of APO, LCO, APO/LCO and APO/LCO/GR composites. The pure APO shows the strong PL emission at 525 nm, which implies the photonic energy level equivalent to that of APO. This equivalent photonic energy implies the potential recombination of photo-excited

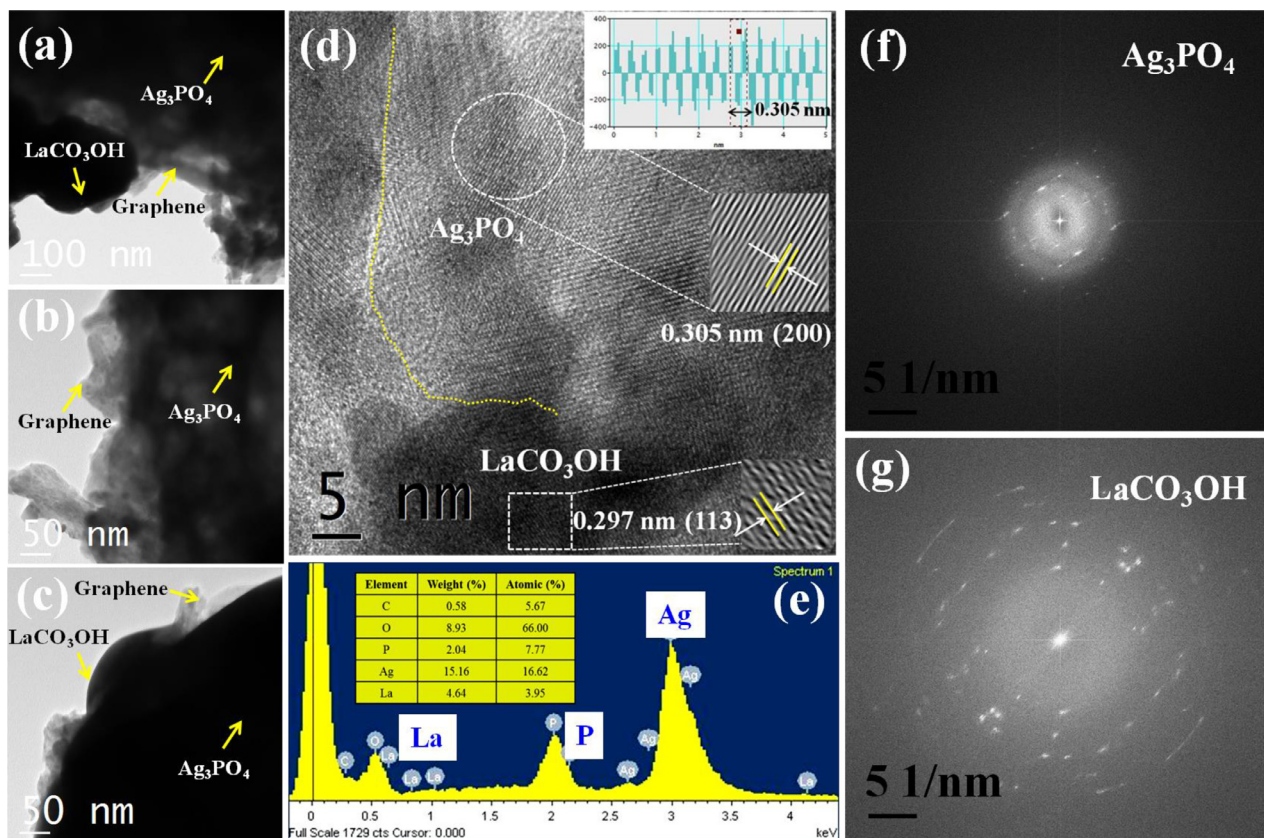


Fig. 5. TEM images of APO/LCO/GR composite (a, b, c), HRTEM (d) and the corresponding fast-Fourier-transform (FFT) patterns (f, g). EDAX profile of composite (e).

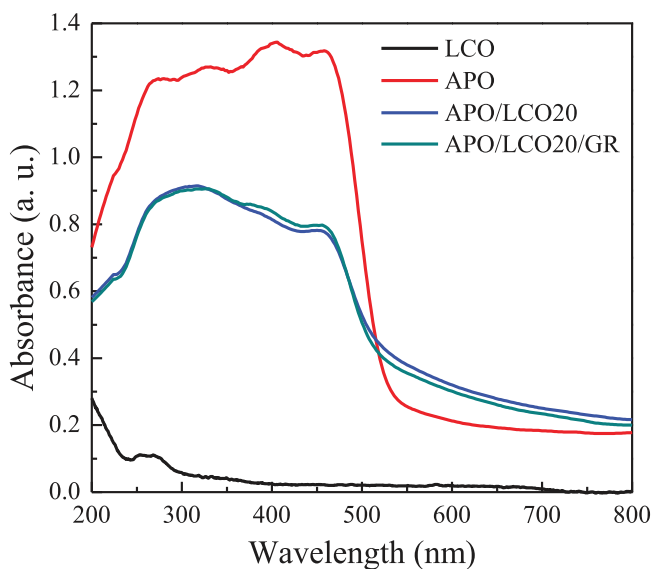


Fig. 6. UV-vis absorption spectra of APO, LCO, APO/LCO and APO/LCO/GR samples.

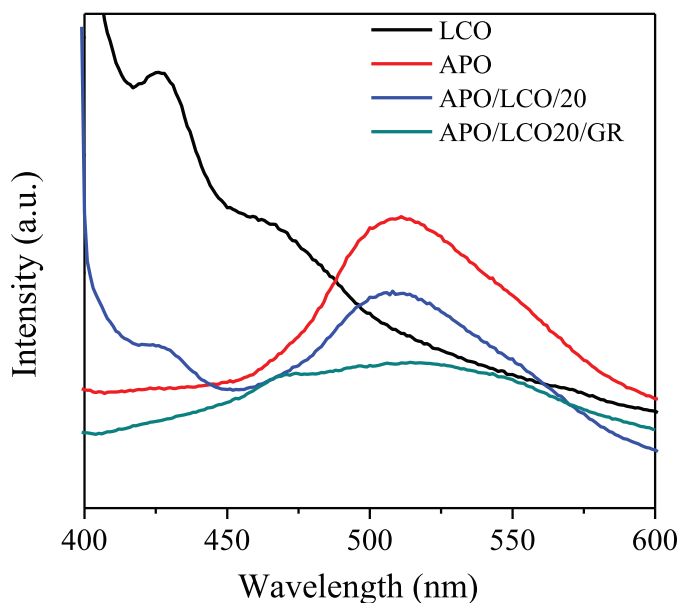


Fig. 7. PL spectra of APO, LCO, APO/LCO and APO/LCO/GR samples.

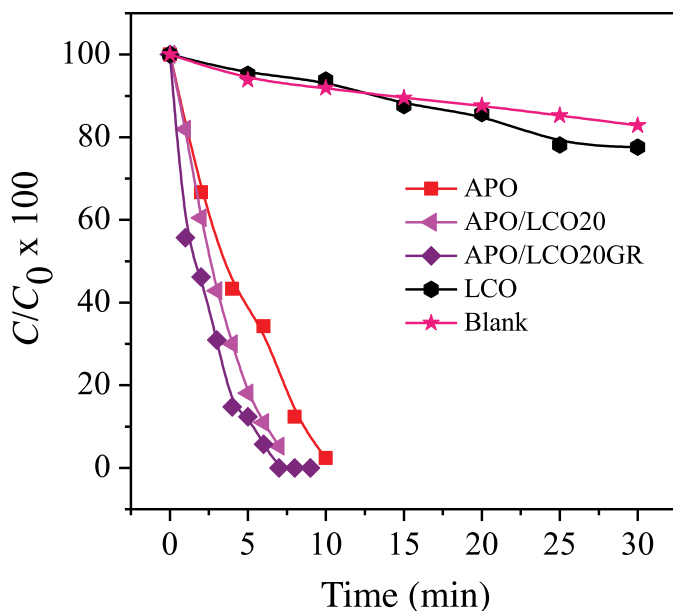
e^-/h^+ at CB and VB of APO. The PL intensity was the highest for the APO case, which indicates the highest recombination rate of the photoexcited e^-/h^+ on the surface of the photocatalyst. The PL intensity of the APO/LCO/GR was drastically reduced which confirms the decrease in the recombination of photo-excited e^-/h^+ at photocatalyst surface, resulting in better photocatalytic performance. It is well known that graphene is an excellent material that transfer electrons efficiently, which facilitates the increase in electronic coupling for the APO/LCO/GR heterostructure composite

and thereby reducing e^-/h^+ recombination. It is apparent that the presence of LCO and GR in the composite improved the separation efficiency as well as the photocatalytic performance.

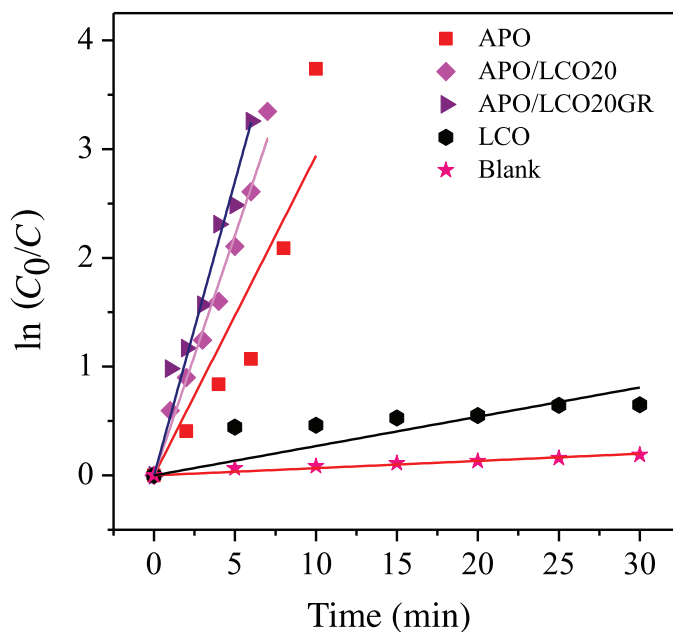
The photocatalytic activity of the samples was evaluated by degradation of methylene blue (MB) under visible light irradiation without the use of a sacrificial reagent. The degradation of MB was monitored by observing the variation of the MB concentration with time under visible light irradiation using UV-vis spectroscopy. For

Table 1. The rate constant (k) values for photocatalytic MB degradation.

Sr. No.	Catalyst	Rate constant (k) for MB degradation (min^{-1})	Std. Dev.
1	APO	0.2939	0.0348
2	LCO	0.0222	0.0025
3	APO/LCO5	0.3299	0.0096
4	APO/LCO10	0.4170	0.0240
5	APO/LCO15	0.4291	0.0242
6	APO/LCO20	0.4436	0.0117
7	APO/LCO25	0.4412	0.0092
8	APO/LCO20/GR1	0.5410	0.0223
9	APO/LCO20/GR2	0.4498	0.0112

**Fig. 8.** Graph of amount of MB remaining after various irradiation times using APO, LCO, APO/LCO, and APO/LCO/GR samples.

comparison, degradation of MB using bare APO, bare LCO, and in the absence of a catalyst (blank) was also examined under similar conditions. The photocatalytic activity was noticeably enhanced with increasing LCO mass ratio in the APO/LCO composite. However, the photocatalytic activity declined with the use of a relatively higher LCO content, i.e., the photocatalytic activity of APO/LCO25 was lower than that of APO/LCO20. This indicates that a higher LCO mass ratio ($x > 20\%$) in the composite structures is unfavorable for the photocatalysis process. The higher content of LCO decreases the light absorption as well as the active sites for the photocatalyst, which degrades the overall photocatalytic activities. Among the APO/LCO composites, highest photocatalytic activity were obtained for APO/LCO20 (Please see, Figures S2 and S3), which we considered optimal. Considering the high efficiency of the APO/LCO20 composite, this sample was selected to integrate with graphene in order to further improve the material properties, stability, and photocatalytic performance. The physicochemical properties of the APO/LCO20/GR composite were significantly enhanced compared to those of pure APO and APO/LCO20 composite, resulting in superior photocatalytic performance of APO/LCO20/GR. In addition, the effect of different graphene loading was investigated to optimize their loading concentration. The comparative results showed that the GR concentration of 1 mg/mL was superior to 2 mg/mL in terms of the photocatalytic performance (see Table 1). Excessive concentration of graphene prevented receiving sufficient light and thus the process of electron/hole generation was hindered. Fig. 8 shows the photocatalytic reaction kinetics

**Fig. 9.** Chemical kinetics study of photocatalytic degradation of MB using APO, LCO, APO/LCO, and APO/LCO/GR samples.

data obtained from photocatalytic degradation of MB using the as prepared samples.

Generally, photocatalytic MB degradation follows the pseudo-first-order reaction and its kinetics could be expressed as,

$$\ln(C_0/C) = kt \quad (1)$$

The apparent rate constants were calculated from the slope of the plot of $\ln(C_0/C)$ versus the irradiation time (Fig. 9), where C_0 is the initial MB concentration and C is the concentration at time t and k is the degradation rate constant. The highest rate constant (k) of 0.541 min^{-1} was estimated for the APO/LCO/GR sample, which was higher than those of APO (0.293 min^{-1}), LCO (0.022 min^{-1}), and APO/LCO20 (0.443 min^{-1}). The highest photocatalytic performance of the APO/LCO20/GR composite could be attributed to the intimate contact between APO and LCO, which facilitates electron-hole (e^-/h^+) separation. Moreover, graphene is known for its large surface area and superior electrochemical properties. Thus, incorporation of graphene improves the surface properties and increases the surface area of the APO/LCO photocatalyst, offering high electron mobility and stability. In the present case, graphene acts as a medium for electron movement and suppresses e^-/h^+ recombination. However, excess graphene reduces the photocatalytic performance of the composite because the higher concentration of graphene has an adverse effect on the light absorption and may obstruct the surface active sites. Therefore, the highest degradation efficiency achieved with the APO-based photocatalyst arises from a constructive effect of both LCO and graphene. Moreover, the degradation of MB in the present case is mainly attributed to the co-catalytic effect of LCO, and the presence of graphene may further assist in MB degradation and in increasing the stability of the photocatalyst.

In order to explain the high photocatalytic efficiency of APO/LCO/GR photocatalyst, we demonstrate a concept of heterojunction construction strategy as a means of improving the efficiency of photocatalytic processes by combining two semiconductors with different band gaps. In the present case, APO is a narrow band gap semiconductor with band gap of 2.46 eV and LCO is a wide band gap semiconductor with band gap of 4.1 eV. A heterojunction photocatalyst represents a conservative approach for ju-

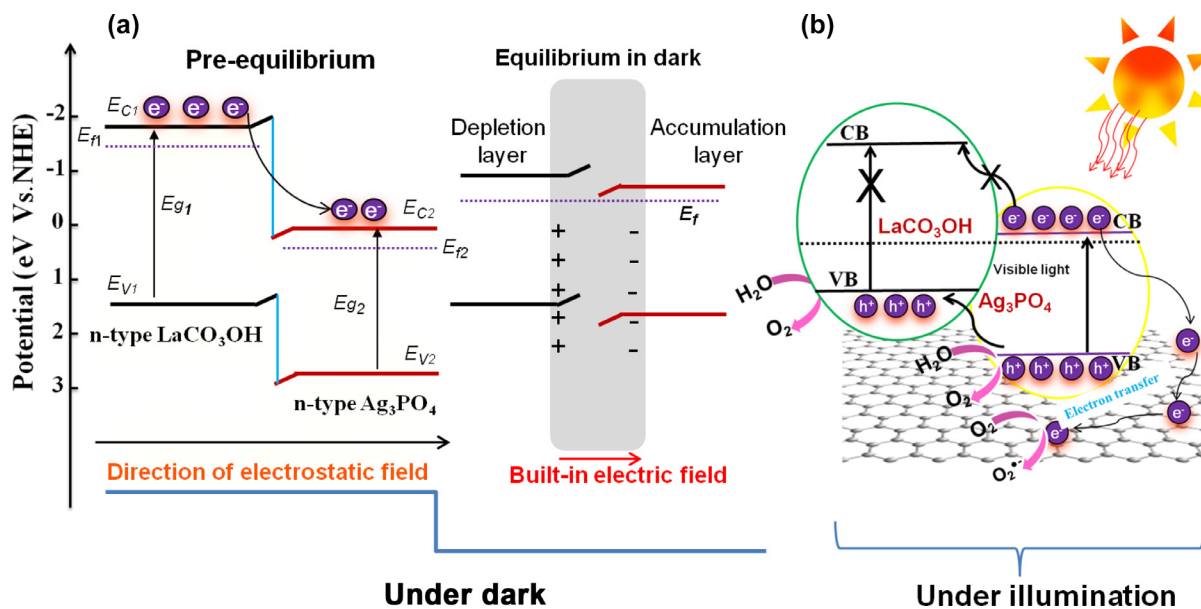


Fig. 10. Mechanism of photocatalytic MB degradation under dark (a) and under illumination (b) conditions using APO/LCO/graphene composite photocatalyst.

icious design of various photocatalysts. Heterojunction photocatalysts offer several advantages such as (i) improved light absorption, (ii) suppression of recombination of photogenerated electrons and holes, (iii) acceleration of surface reactions, (iv) improved stability of the photocatalyst, and (v) increased surface area of the photocatalyst via loading of high surface area materials. A schematic representation of the mechanism of photocatalytic MB degradation in the presence of APO/LCO/GR photocatalyst is shown in Fig. 10.

In APO/LCO/GR photocatalyst, the APO semiconductor absorbs visible light and undergoes photo-excitation to produce e^-/h^+ pairs. In contrast, LCO cannot absorb visible light due to its wide band gap; however, LCO possesses negative conduction and valence band levels compared to that of APO [27]. The CB level of LCO is composed of 4f states of La atom with negative reduction potential, whilst the VB level is mainly formed by O 2p orbitals, which is positive enough to carry out oxidation processes [27]. The appropriate band level alignment of LCO is beneficial for separation of e^-/h^+ pairs at the interface of the APO/LCO. In the present case, both the APO and LCO are n-type semiconductors with different Fermi energy levels close to the CB. As shown in Fig. 10(a), when the n-n APO-LCO heterojunction is formed and kept under dark condition, electrons will flow from LCO to APO, since the CB of LCO is more negative (-0.87 vs. NHE) than APO. Thus, an internal electrostatic field is established at the n-n interface which directed the continuous flow of electron causing a depletion layer (positively charged region) on LCO side and accumulation layer (negatively charged region) on APO side [20,40]. This process continues until the equilibrium is attained (Equalized Fermi level E_f) with generation of built in electric field directed from LCO to APO [41]. When heterojunction is illuminated by solar light (Fig. 10b), the generated built-in field promotes the formation of photogenerated charge carriers in APO, which will flow the electrons towards LCO [41]. However, due to presence of more negative CB of LCO, the electrons in the CB of APO cannot be migrated to CB of LCO [39,40]. Instead, the photogenerated electrons gather at the interface of APO and LCO. It is important to note that the LCO/APO heterostructure is wrapped in the graphene sheets. Therefore, the accumulated electrons at the interface will be further migrated to the graphene sheets very rapidly since the mobility of electrons on graphene is very high due to the specific n-conjugated structure. The shuttled electrons on the surface of

the graphene sheet react with absorbed oxygen to form oxidants such as superoxide ions ($\cdot O_2^-$). Thereby, the GR sheets separate the electrons from APO and hinder the probability of photoreduction of Ag in APO (photocorrosion of Ag₃PO₄), which is the major obstruction to achieve high efficiency and stability of pure APO photocatalyst. Meanwhile, since, LCO is in intimate contact with APO, photoexcited holes from the VB of APO would migrate to the less positive VB of LCO and further react with the absorbed H₂O molecules to form active oxidants such as hydroxyl radicals ($\cdot OH$). Eventually, the generated active radical species ($\cdot O_2^-$ and $\cdot OH$) decompose the MB dye molecules into CO₂ and H₂O [42]. More importantly, the APO/LCO/GR photocatalyst significantly accelerates photocatalytic degradation of MB via the co-catalytic effect of LCO, and the presence of GR on the APO/LCO heterostructure effectively prevents decomposition of APO into metallic Ag, thus offering better stability and photocatalytic efficiency. Further, the stability of the as-synthesized composite photocatalyst was evaluated by the re-use of the photocatalyst in three consecutive cycles and the XRD patterns of the reused sample were recorded. The XRD patterns of the APO/LCO/GR composite before and after the photocatalysis experiments were identical, indicating suppression of photocorrosion of APO and improved stability of the material (see Figures S4 and S5). The recyclability of the APO/LCO/GR composite suggests that the photocatalytic activity remained robust even after the multiple uses for MB photodegradation (see Table S1).

4. Conclusions

An efficient heterojunction APO/LCO/GR photocatalyst was fabricated by a simple in situ wet chemical method. The photocatalytic degradation of MB in the presence of the APO/LCO/GR photocatalyst was evaluated. Among the studied photocatalysts, the APO/LCO20/GR composite photocatalyst exhibited superior photocatalytic activity (rate k : 0.541 min⁻¹) for MB degradation. The catalyst efficiency of APO/LCO20/GR is significantly higher than that of APO (0.293 min⁻¹), LCO (0.022 min⁻¹), and APO/LCO20 (0.443 min⁻¹). This enhanced photocatalytic activity is ascribed to the constructive effect derived from the co-catalytic effect of LCO, resulting in accelerated charge separation, and the presence of GR effectively prevents decomposition of Ag₃PO₄ into metallic Ag (photocorrosion), offering better stability. Overall, the high stability

and high efficiency of the APO/LCO/GR sample should make this sample effective for decomposition of organic pollutants in industrial wastewater.

Acknowledgments

Authors would like to thank Department of Electronics and Information Technology (DeitY, New Delhi) for financial support. Authors wish to thank Nanocrystalline Material and Glass Laboratory, C-MET Pune for their generous help. Authors also acknowledge the support from UGC-SAP, DST-FIST Department of Chemistry, Shivaji University Kolhapur. The author acknowledges Prof. S. W. Gosavi, Department of Physics, Savitribai Phule Pune University for providing the technical support. This research was partially supported by the Commercialization Promotion Agency for R&D Outcomes (COMPA) funded by the Ministry of Science, ICT and Future Planning (MISP) and NRF-2013R1A2A2A05005589. S.S.Y. expresses his thanks to the support made by King Saud University, Vice Deanship of Research Chairs.

Supplementary materials

Supplementary material associated with this article can be found, in the online version, at [doi:10.1016/j.jechem.2016.05.004](https://doi.org/10.1016/j.jechem.2016.05.004).

References

- [1] C. Chen, W. Ma, J. Zhao, *Chem. Soc. Rev.* 39 (2010) 4206–4219.
- [2] D. Zhang, *Monatsh. Chem.* 143 (2012) 729–738.
- [3] D. Zhang, F. Zeng, *J. Mater. Sci.* 47 (2012) 2155–2161.
- [4] Y. Shi, K. Zhou, B. Wang, S. Jiang, X. Qian, Z. Gui, R.K. Yuen, Y. Hu, *J. Mater. Chem. A* 2 (2014) 535–544.
- [5] W. Tu, Y. Zhou, Z. Zou, *Adv. Funct. Mater.* 23 (2013) 4996–5008.
- [6] J. Zhang, S.Z. Qiao, L. Qi, J. Yu, *Phys. Chem. Chem. Phys.* 15 (2013) 12088–12094.
- [7] N.S. Chaudhari, A.P. Bhirud, R.S. Sonawane, L.K. Nikam, S.S. Warule, V.H. Rane, B.B. Kale, *Green. Chem.* 13 (2011) 2500–2506.
- [8] M. Hashim, C. Hu, X. Wang, B. Wan, J. Xu, *Mater. Res. Bull.* 47 (2012) 3383–3389.
- [9] B.B. Kale, J.O. Baeg, S.M. Lee, H. Chang, S.J. Moon, C.W. Lee, *Adv. Funct. Mater.* 16 (2006) 1349–1354.
- [10] R. Asahi, T. Morikawa, T. Ohwaki, K. Aoki, Y. Taga, *Science* 293 (2001) 269–271.
- [11] N. Zhang, S. Ouyang, T. Kako, J. Ye, *Chem. Commun.* 48 (2012) 1269–1271.
- [12] Y. Bi, S. Ouyang, N. Umezawa, J. Cao, J. Ye, *J. Am. Chem. Soc.* 133 (2011) 6490–6492.
- [13] L. Xu, W.-Q. Huang, L.-L. Wang, G.-F. Huang, P. Peng, *J. Phys. Chem. C* 118 (2014) 12972–12979.
- [14] C.-T. Dinh, T.-D. Nguyen, F. Kleitz, T.-O. Do, *Chem. Commun.* 47 (2011) 7797–7799.
- [15] Z. Yi, J. Ye, N. Kikugawa, T. Kako, S. Ouyang, H. Stuart-Williams, H. Yang, J. Cao, W. Luo, Z. Li, *Nat. Mater.* 9 (2010) 559–564.
- [16] R. Rajendran, M. Pudukudy, S. Sohila, Z. Yaakob, M.S.A. Rahaman, *J. Mater. Sci.: Mater. Electron.* 25 (2014) 4755–4759.
- [17] Z. Lou, B. Huang, Z. Wang, R. Zhang, Y. Yang, X. Qin, X. Zhang, Y. Dai, *CrystEngComm* 15 (2013) 5070–5075.
- [18] H. Wang, L. He, L. Wang, P. Hu, L. Guo, X. Han, J. Li, *CrystEngComm* 14 (2012) 8342–8344.
- [19] W. Yao, B. Zhang, C. Huang, C. Ma, X. Song, Q. Xu, *J. Mater. Chem.* 22 (2012) 4050–4055.
- [20] S.S. Patil, M.S. Tamboli, V.G. Deonikar, G.G. Umarji, J.D. Ambekar, M.V. Kulkarni, S.S. Kolekar, B.B. Kale, D.R. Patil, *Dalton Trans* 44 (2015) 20426–20434.
- [21] Z. Cui, M. Si, Z. Zheng, L. Mi, W. Fa, H. Jia, *Catal. Commun.* 42 (2013) 121–124.
- [22] J. Li, Z. Liu, Z. Zhu, *J. Alloys Compd* 636 (2015) 229–233.
- [23] S.S. Patil, D.R. Patil, S.K. Apte, M.V. Kulkarni, J.D. Ambekar, C.-J. Park, S.W. Gosavi, S.S. Kolekar, B.B. Kale, *Appl. Catal. B: Environ.* 190 (5) (2016) 75–84.
- [24] X. Yang, J. Qin, Y. Jiang, R. Li, Y. Li, H. Tang, *RSC Adv.* 4 (2014) 18627–18636.
- [25] Z. Chen, W. Wang, Z. Zhang, X. Fan, *The J. Phys. Chem. C* 117 (2013) 19346–19352.
- [26] J. Guo, S. Ouyang, P. Li, Y. Zhang, T. Kako, J. Ye, *Appl. Catal., B: Environ.* 134 (2013) 286–292.
- [27] B. Pan, Q. Xie, H. Wang, J. Zhu, Y. Zhang, W. Su, X. Wang, *J. Mater. Chem. A* 1 (2013) 6629–6634.
- [28] X. Guan, L. Guo, *ACS Catal.* 4 (2014) 3020–3026.
- [29] X. Yang, H. Cui, Y. Li, J. Qin, R. Zhang, H. Tang, *ACS Catal.* 3 (2013) 363–369.
- [30] Q. Xiang, D. Lang, T. Shen, F. Liu, *Appl. Catal. B: Environ.* 162 (2015) 196–203.
- [31] X. Yang, J. Qin, Y. Jiang, K. Chen, X. Yan, D. Zhang, R. Li, H. Tang, *Appl. Catal. B: Environ.* 166 (2015) 231–240.
- [32] X. Yang, Z. Chen, J. Xu, H. Tang, K. Chen, Y. Jiang, *ACS Appl. Mater. Interfaces* 7 (28) (2015) 15285–15293.
- [33] X. Yang, H. Tang, J. Xu, M. Antonietti, M. Shalom, *ChemSusChem* 8 (8) (2015) 1350–1358.
- [34] X. Chen, X. Huang, Z. Yi, *Chem. Eur. J.* 20 (2014) 17590–17596.
- [35] Y. He, L. Zhang, B.T. Teng, M. Fan, *Environ. Sci. Technol.* 49 (1) (2014) 649–656.
- [36] D.C. Marcano, D.V. Kosynkin, J.M. Berlin, A. Sinitskii, Z. Sun, A. Slesarev, L.B. Alemany, W. Lu, J.M. Tour, *ACS nano* 4 (2010) 4806–4814.
- [37] Y.-S. Xu, W.-D. Zhang, *Dalton Trans.* 42 (2013) 1094–1101.
- [38] W.-S. Wang, H. Du, R.-X. Wang, T. Wen, A.-W. Xu, *Nanoscale* 5 (2013) 3315–3321.
- [39] Y. Bi, S. Ouyang, J. Cao, J. Ye, *Phys. Chem. Chem. Phys.* 13 (2011) 10071–10075.
- [40] N. Liang, J. Zai, M. Xu, Q. Zhu, X. Wei, X. Qian, *J. Mater. Chem. A* 2 (2014) 4208–4216.
- [41] M. Xu, T. Ye, F. Dai, J. Yang, J. Shen, Q. He, W. Chen, N. Liang, J. Zai, X. Qian, *ChemSusChem* 8 (2015) 1218–1225.
- [42] S.S. Patil, M.G. Mali, M.S. Tamboli, D.R. Patil, M.V. Kulkarni, H. Yoon, H. Kim, S.S. Al-Deyab, S.S. Yoon, S.S. Kolekar, *Catal. Today* 260 (2016) 126–134.